

Accelerated calculation of configurational free energy using a combination of reverse Monte Carlo and neural network models: Adsorption isotherm for 2D square and triangular lattices

Akash Kumar Ball^a, Swati Rana^b, Gargi Agrahari^a and Abhijit Chatterjee^{a*}

^a **Department of Chemical Engineering, Indian Institute of Technology Bombay, Mumbai 400076, India**

^b **Department of Energy Science and Engineering, Indian Institute of Technology Bombay, Mumbai 400076, India**

*Email: abhijit@che.iitb.ac.in

ABSTRACT

We demonstrate the application of artificial neural network (ANN) models to reverse Monte Carlo based thermodynamic calculations. Adsorption isotherms are generated for 2D square and triangular lattices. These lattices are considered because of their importance to catalytic applications. In general, configurational free energy terms that arise from adsorbate arrangements are challenging to handle and are typically evaluated using computationally expensive Monte Carlo simulations. We show that a combination of reverse Monte Carlo (RMC) and ANN model can provide an accurate estimate of the configurational free energy. The ANN model is trained/constructed using data generated with the help of RMC simulations. Adsorption isotherms are accurately obtained for a range of adsorbate-adsorbate interactions, coverages and temperatures within few seconds on a desktop computer using this method. The results are

validated by comparing to MC calculations. Additionally, H adsorption on Ni(100) surface is studied using the ANN/RMC approach.

Keywords: Adsorption isotherm, reverse Monte Carlo, short-ranged order, thermodynamics, machine learning

1. Introduction

In this current era of artificial intelligence, machine learning (ML) based models are increasingly being used in molecular simulations. ML has been applied to a variety of problems ranging from quantum mechanical calculations¹, to the construction of classical interatomic potentials²⁻⁵, structure-prediction and materials design^{6,7}, and predicting thermo-physical properties⁸ and activation barriers⁹. An artificial neural network (ANN) model is often used in these applications. The popularity of ANN arises from its general functional form, which enables users to train the ANN model to high-dimensional nonlinear data. The ANN model is simply a computational tool which needs to be combined with a systematic theoretical framework/strategy so that a time-consuming molecular simulation can be replaced without incurring significant loss of accuracy. While the role of the ANN model is to act as a computationally-inexpensive surrogate model, it is the framework that provides the basis for such calculations. Recently, ML has been applied to modelling of the free energy¹⁰ and for thermodynamic calculations¹¹⁻¹³. In this work, we discuss a different strategy for thermodynamic calculations which involves the combination of reverse Monte Carlo (RMC) and ANN models. The ANN model is used to solve a detailed balance equation.

The problem is of general interest to the area of statistical thermodynamics. Free energies associated with ideal gas, translation, rotation, vibration, electronic and nuclear degrees of freedom can be evaluated with reasonable accuracy. This leaves the challenging part, namely, the configurational free energy, which arises from the ordering/arrangement of molecules within the system^{14–21}. A popular approach is the use of Metropolis Monte Carlo (MC) simulations^{22–25}. In general, many configurations need to be sampled in MC before the calculation is converged. Thus, MC is computationally expensive and usually only a limited number of conditions can be simulated. MC calculations also become computationally prohibitive as the system size increases. The use of free energy extrapolations/expansions can help improve the efficiency^{26–28}. In this paper, the configurational free energy is evaluated using the combination of RMC and ANN model, which completely bypasses the need for MC without compromising on accuracy.

The RMC-based framework for thermodynamic calculations^{29–31} was recently introduced by the authors. We study adsorption on 2D lattices shown in Figure 1a and b. Such lattices are typically encountered with the face centered cubic (100) and (111) surfaces of metal catalysts. It should be noted that several machine learning models^{32–38} have been developed to study adsorption phenomena on more complex systems with machine learning algorithms that are more sophisticated than the ANN model used here. Nonetheless, our approach extends the application of RMC to adsorption studies. This is because traditionally RMC has been mainly employed to create 2D/3D structural models for liquids and solids that are consistent with experimental scattering data^{39–47}, and not for thermodynamic calculations. The combined RMC-ANN modelling approach is shown to be accurate and orders-of-magnitude faster than MC. MATLAB codes with

compact ANN models are provided in Supporting Information to demonstrate how configurational terms are evaluated in few seconds on a desktop computer.

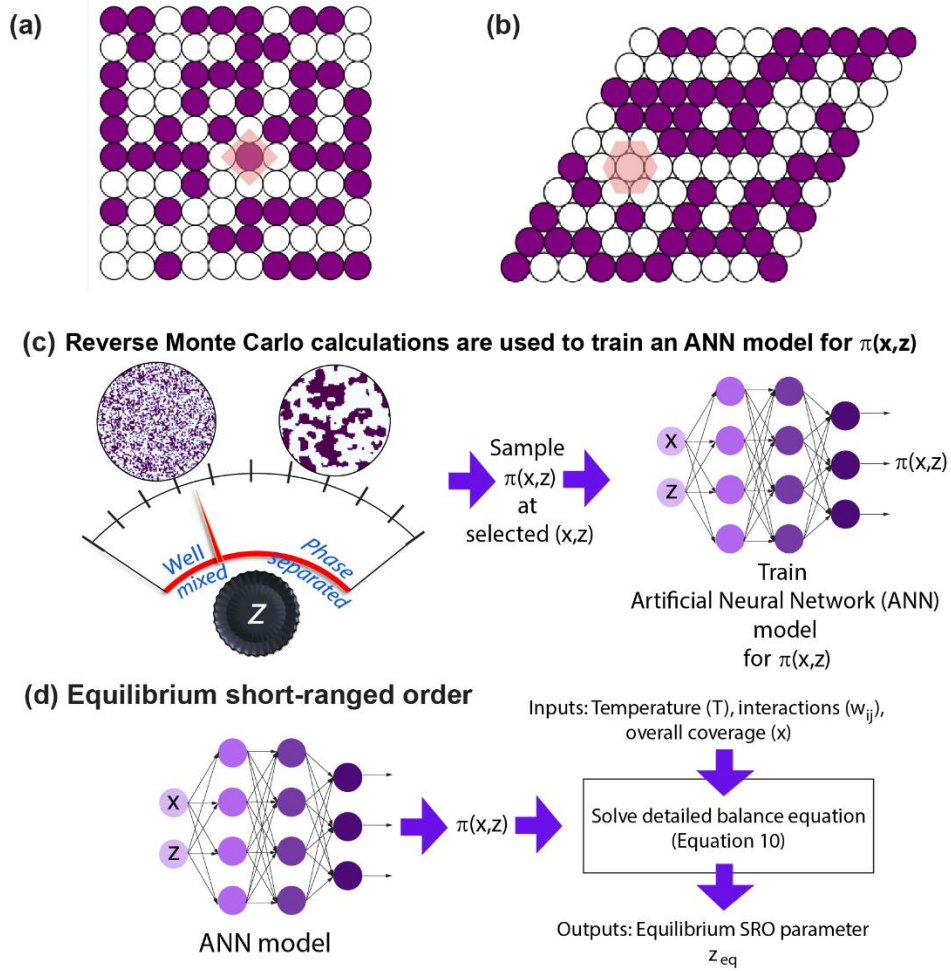


Figure 1: (a) Square and (b) triangular lattices. Filled/open circles denotes occupied/vacant sites. (c) Flowchart for the construction of ANN model for $\pi(x, z)$. (d) Flowchart for determining short-ranged order z_{eq} at equilibrium.

The basic theory is developed in Section 2. In Section 3, we discuss the RMC algorithm, construction procedure of ANN, as well as GCMC calculations. In Section 4, we assess the accuracy of our ANN model. We validate our ANN-RMC approach by generating adsorption isotherms and making comparisons to grand-canonical Monte-Carlo (GCMC). Isotherm for the H/Ni(100) system is generated. Conclusions are provided in Section 5.

2. Theory

Consider a 2D lattice system denoted as A_xV_{1-x} , where A is the adsorbed species, V represents vacant sites and x is the adsorbate coverage. N_A, N_V and N_t are the number of occupied, vacant, and total sites, respectively, $N_t = N_A + N_V$ and $x = N_A/N_t$. Adsorbed A particles interact with first nearest neighbors (1NN) interactions. w is the interaction energy for an $A - A$ pair. Periodic boundary conditions are employed. The Hamiltonian for the system is

$$H(\sigma; N_A, N_t, T) = \sum_{\langle i,j \rangle} w \sigma_i \sigma_j. \quad (1)$$

σ_i is the occupation at site i . σ_i is 1 when the site is occupied, and zero otherwise. $\langle i,j \rangle$ in Equation (1) implies pairs of 1NN sites $i - j$.

2.1 Chemical potential calculation using environment distribution

Different local particle arrangements are possible (see Figure 1). ϵ denotes the number of A atoms in the first coordination shell. The probability associated with such ϵ when the central site

is occupied by A is $\pi_{AA,eq}(\epsilon)$.^a The subscript eq implies equilibrium when N_A , N_t and T are constant. Similarly, $\pi_{VA,eq}(\epsilon)$ is the distribution around a V site, such that $\pi_{AA,eq}(\epsilon) \neq \pi_{VA,eq}(\epsilon)$.

From Ref. ³⁰, the chemical potential is

$$\Delta\mu(x, T) = k_B T \ln \frac{x}{1-x} - k_B T \ln \langle \exp(-\beta \Delta U_\epsilon) \rangle_x \quad (2)$$

where $\beta = (k_B T)^{-1}$, k_B is the Boltzmann constant, T is the temperature, and

$$\langle \exp(-\beta \Delta U_\epsilon) \rangle_x = \sum_{\epsilon=0}^c \pi_{VA,eq}(\epsilon) \exp(-\beta \Delta U_\epsilon). \quad (3)$$

The coordination number c in the 1NN shell is 4 for square lattice and 6 for triangular lattice. ΔU_ϵ is the energy change when an A particle is inserted at a vacant site, i.e., $\Delta U_\epsilon = \epsilon w$. Alternatively, $\Delta\mu$ is calculated by removing an adsorbed A , i.e.,

$$\Delta\mu(x, T) = k_B T \ln \frac{x}{1-x} + k_B T \ln \langle \exp(-\beta \Delta U'_\epsilon) \rangle_x. \quad (4)$$

In such a case, the excess term

$$\langle \exp(-\beta \Delta U'_\epsilon) \rangle_x = \sum_{\epsilon=0}^c \pi_{AA,eq}(\epsilon) \exp(-\beta \Delta U'_\epsilon). \quad (5)$$

Here, $\Delta U'_\epsilon$ is the energy change associated with the removal of an A particle with environment ϵ from an occupied site.

2.2 Local environment, probability distribution and connection to short-ranged order

From equation (2)-(5), we find that $\pi_{AA,eq}(\epsilon)$ and $\pi_{VA,eq}(\epsilon)$ are key quantities for estimating thermodynamic properties. A procedure to calculate $\pi_{AA,eq}(\epsilon)$ and $\pi_{VA,eq}(\epsilon)$ is needed. We

^a In general, $\pi_{ij}(\epsilon)$ is the probability of having ϵ number of j atoms around central site with i atom.

assume that the 2D atomic arrangements at the surface are determined by x and a short-ranged order (SRO) parameter $z^{39,48-50}$. z is the average fraction of 1NN sites around A occupied by A particles.²⁹ z determines the local ordering. See Figure 1c for types of arrangements associated with different values of z . For random arrangement of the adsorbed particles $z = x$. Separate A - and B -rich regions are formed when $z \approx 1$.

How π_{AA} and π_{VA} varies with x and z is ascertained using RMC. x and z are the main inputs to RMC. Initially, a 2D lattice configuration random A arrangement is created. Trial moves are attempted wherein the positions of a randomly chosen pair of A and V sites are swapped with an acceptance probability. The procedure is repeated till the target number of $A - A$ first nearest neighbor pairs $N_{AA,target} = \frac{czN_A}{2}$ is achieved. RMC calculations are independent of w and T .

2D RMC configurations obtained at selected values of (x, z) are used to evaluate $\pi_{AA}(\epsilon; x, z)$ and $\pi_{VA}(\epsilon; x, z)$. Figure 1c shows a flowchart for the construction of the ANN model for $\pi(\epsilon; x, z)$. The ANN model provides a closed form expression for $\pi(\epsilon; x, z)$, which is not generally available for 2D lattice systems.

2.3 Environment distribution at equilibrium using the Detailed Balance Equation

We write $\pi_{AA,eq}(\epsilon) \equiv \pi_{AA}(\epsilon; x, z_{eq})$ and $\pi_{VA,eq}(\epsilon) \equiv \pi_{VA}(\epsilon; x, z_{eq})$. This implies that the equilibrium distribution is the one obtained from RMC at (x, z_{eq}) . The goal is to determine z_{eq} , the SRO parameter value at equilibrium, by solving a detailed balance equation.

Consider a swap move $A(\epsilon) + V(\epsilon') \rightleftharpoons A(\epsilon') + V(\epsilon)$, where $A(\epsilon)$ implies an A with environment ϵ . For $\epsilon < \epsilon'$, the forward direction (right arrow) results in an A particle moving into an A -rich environment. The net probability flux for this combination $\epsilon - \epsilon'$ is

$$f(\epsilon, \epsilon'; x, z) = p(A(\epsilon), V(\epsilon'))\Gamma_r - p(A(\epsilon'), V(\epsilon))\Gamma_l. \quad (6)$$

Γ_r and Γ_l are transition probabilities in the right and left direction, respectively. The probability of selecting the pair $A(\epsilon) - V(\epsilon')$ is $p(A(\epsilon), V(\epsilon')) = \pi_{AA}(\epsilon)\pi_{VA}(\epsilon')$. Similarly, the probability of selecting the pair $A(\epsilon') - V(\epsilon)$ is $p(A(\epsilon'), V(\epsilon)) = \pi_{AA}(\epsilon')\pi_{VA}(\epsilon)$. The ratio $\frac{p(A(\epsilon'), V(\epsilon))}{p(A(\epsilon), V(\epsilon'))} = \exp(-\beta\Delta U)$ where $\Delta U = w(\epsilon' - \epsilon)$ is the energy change of the system along the right arrow. Γ_r and Γ_l are expressed analogous to the standard Metropolis acceptance criterion⁵¹ as

$$\Gamma_r = \min(1, \exp(-\beta\Delta U)) \quad (7)$$

and

$$\Gamma_l = \min(1, \exp(\beta\Delta U)). \quad (8)$$

The overall net probability flux obtained by considering all pair environments $\epsilon - \epsilon'$

$$N(x, z) = \left| \sum_{\epsilon < \epsilon'} f(\epsilon, \epsilon'; x, z) \right|. \quad (9)$$

is zero at equilibrium. Finally, we write the detailed balance equation as

$$N(z_{eq}; x, w, T) = 0. \quad (10)$$

A crucial point is that $\pi(\epsilon; x, z)$ can be employed with a variety of interactions, temperatures and coverages. This makes the ANN model versatile. When x , total number of lattice sites N_t , temperature T and the adsorbate-adsorbate interactions w are specified, the goal is to identify

the value of $z_{eq}(x, w, T)$ where detailed balance is satisfied. Equation (10) is solved using a gradient-based Newton method. The flowchart is shown in Figure 1d. The approach is computationally less demanding than MC since it involves root-finding. Thereafter, $\Delta\mu$ is calculated using Equation (2) or (4).

ANN offers some significant implementational advantages compared to our earlier approach. Earlier, $\pi(\epsilon; x, z)$ used to be stored in the form of look-up tables^{29–31}. Look-up tables can be unwieldy, whereas ANN is compact. A Delaunay triangulation-based interpolation scheme was employed with the look-up table to calculate π at any given x, z . A fine-grid in $x - z$ space³¹ is needed to lower the interpolation error. ANN requires RMC structures at fewer number of $x - z$ points as shown later. Moreover, the interpolated probability from look-up tables can contain noise, which prohibits the use of gradient-based Newton method for root finding.

3. Computational details

3.1 RMC algorithm

A brief description of the RMC algorithm is provided. A periodic lattice of size 325×325 with $N_t = 105,625$ is employed. A random arrangement of A is prepared, such that initially the number of $A - A$ bonds $N_{AA} = \frac{1}{2} N_A c x$. The steps in RMC are²⁹:

Step 1: N_{AA} is calculated for current configuration. The distance from the target structure $d^2 =$

$|N_{AA} - N_{AA,target}|^2$ is calculated.

Step 2: A pair of A and V sites are chosen randomly and their positions are swapped. The new number of $A - A$ bonds $N_{AA,n}$ as well as the new distance to target structure d_n^2 is evaluated.

Step 3: The acceptance probability is calculated as

$$p_{acc} = \min(1, \exp(d^2 - d_n^2)). \quad (11)$$

The lattice structure is updated if the move is accepted. Else, the old configuration remains.

Step 4: The RMC calculation is stopped once π_{AA} and π_{VA} become stationary. Otherwise, steps 1-4 are repeated.

Snapshots from RMC are shown in Figure 2. Usually, ordering behavior is expected when $z < x$.

Random structures are obtained with $x = z$. Clustering of A is observed with increasing z .

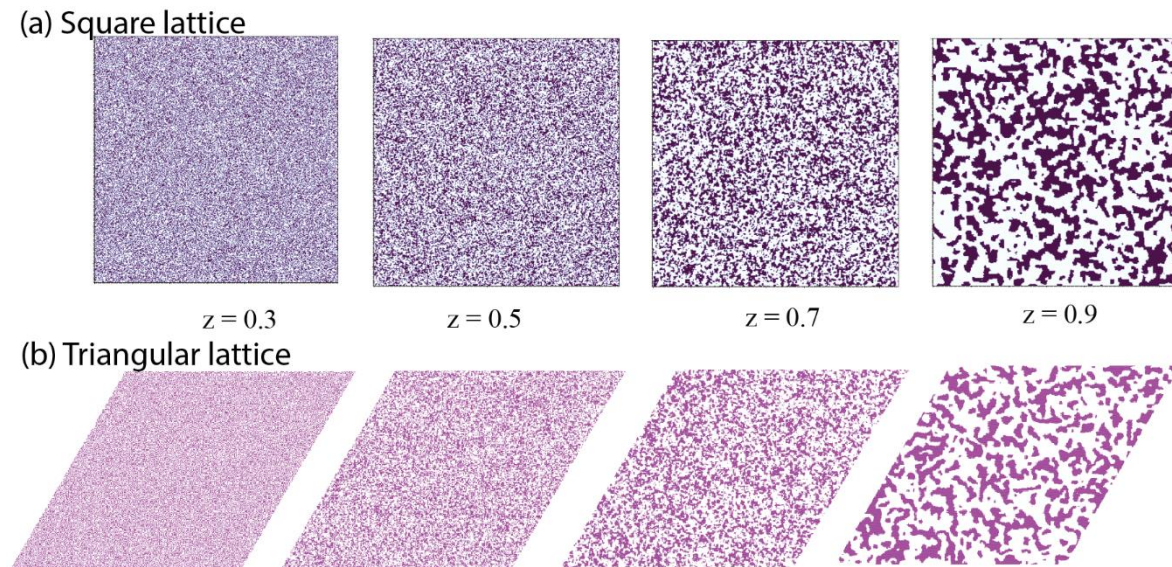


Figure 2: RMC structures obtained with $x = 0.4$ and varying z . (a) Square and (b) triangular lattice. Purple dots indicate A -sites.

3.2 ANN construction

The goal here is to “learn” a function that maps x and z to probability distributions discussed earlier. The function is inferred using the data $\pi_{AA}(\epsilon; x, z)$ and $\pi_{VA}(\epsilon; x, z)$, $\epsilon \in [0, c]$ collected using RMC. A large number of supervised learning methods are available⁵². However, because of our previous experience with ANN models^{9,53}, we have preferred ANN. Figure 3a shows the architecture used to obtain a probability distribution. The inputs to the ANNs are x and z . There are $c + 1$ different ϵ values. One ANN can predict $\pi_{AA}(\epsilon; x, z)$ for a given ϵ . Thus, $c + 1$ ANNs are used. The situation is similar for $\pi_{VA}(\epsilon)$. Finally, $\pi_{AA}(\epsilon)$ or $\pi_{VA}(\epsilon)$ is normalized so that $\sum_{\epsilon=0}^c \pi_{AA}(\epsilon) = 1$ and $\sum_{\epsilon=0}^c \pi_{BA}(\epsilon) = 1$.

375 points sampled in the $x - z$ space for training and validation are shown in Figure 3b. Such a dataset was not available previously. RMC calculations were performed for the square and triangular lattice separately. Although in principle $x, z \in [0, 1]$, certain parts of the space are not accessible with RMC. For instance, the values of $z < 1.2636x - 0.263$ are not topologically possible especially when $x > 0.2$, as this would require low number of A pairs despite the high fraction of A particles in the lattice. This approximate boundary is shown as a solid blue line in Figure 3b. Similarly, configurations with z values above the dashed blue line in Figure 3b cannot be created with the size of the lattice chosen in the present study especially when x is low, as it will require almost every A to be surrounded by A neighbor although the fraction of V sites is large. The inaccessible region is approximately $z > 0.334x^3 - 0.6197x^2 + 0.4039x + 0.882$. This boundary can be shifted towards higher z by selecting a lattice of larger size.

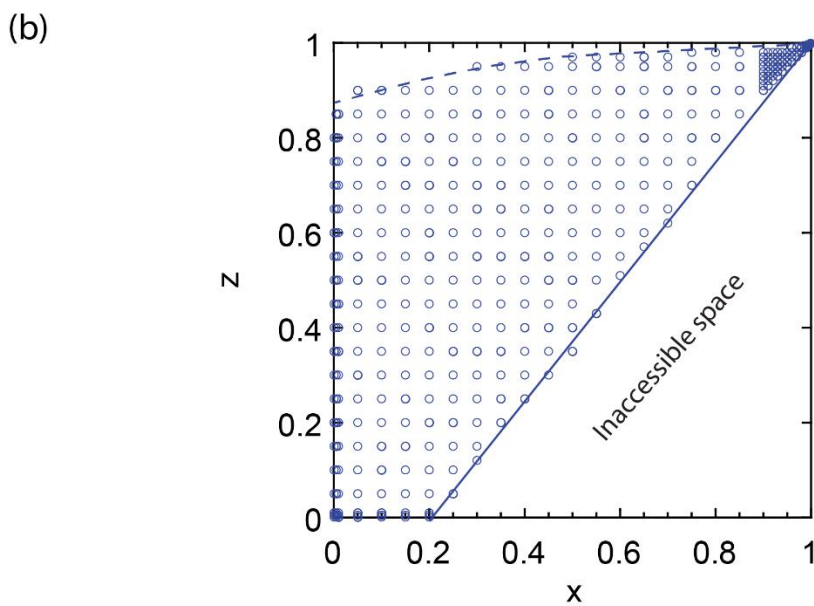
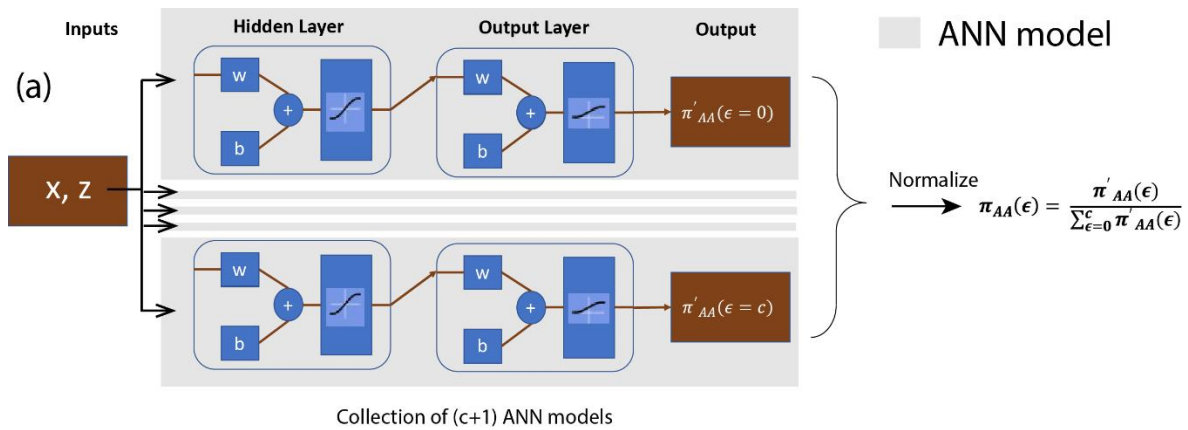


Figure 3: (a) ANN model structure: each model gives the probability for a particular $\epsilon, \epsilon \in [0, c]$. The output is normalized so that sum of probabilities is one. (b) $x - z$ space sampled using RMC. Each circle denotes one RMC calculation.

The ANN training is performed using feedforward neural network with 1 to 2 hidden layers in MATLAB (see Section S1 of Supporting Information). The number of neurons in the hidden layer(s) is allowed to vary between 5 to 10. We begin with a single neuron and then keep adding

neurons until the accuracy of training and validation increases. Beyond a certain point, the accuracy of validation decreases with additional neurons due to overfitting. At this point, we obtain the optimal number of neurons. Hyperbolic tangent (tanh) is used as the activation function in the hidden layer(s) due to its differentiability over the entire domain. Sigmoid function is used in the output layer so that the probabilities lie between 0 and 1. The probability distribution dataset which is used to train and validate ANN models does not require additional scaling as it is already normalized. Mean Squared Error (MSE) is used as loss function while training the ANN models. The weights and biases of ANNs are initialized using Nguyen-Widrow initialization algorithm⁵⁴.

The training set is generated by random selection of 70 % data of the original dataset, the rest is incorporated in the validation set. The dataset consists of 375 datapoints. This is far smaller than earlier datasets used with interpolation method – such datasets contained >800 points³¹. A Levenberg-Marquardt backpropagation algorithm is used for minimizing the mean-squared error (MSE) between predicted and actual probability. The number of epochs is set to be 10^5 and the tolerance for gradient in MSE is 10^{-7} . Section S1 of Supporting Information provides details of the learning curve, MAE, MSE reduction behavior and cross-validation.

3.3 GCMC calculations

Grand-canonical ensemble (constant $\Delta\mu$, T , N_T) MC calculations are performed to determine x as a function of $\beta\Delta\mu$ for different interactions w . Two types of starting configurations are

considered: only V (loading) and only A present (unloading). The GCMC calculation consists of swap, insertion and deletion trial moves.⁵⁵ Acceptance criterion is shown in Table 1.

Table 1: Probability acceptance criterion of different trial moves. ΔU denotes the energy difference between the new and the old configuration.

Type of trial move	Percentage of moves attempted	Acceptance probability (p_{acc})
Swap	60	$\min(1, \exp(-\beta\Delta U))$
Insertion	20	$\min\left(1, \frac{N_B}{N_A + 1} \exp[\beta(\Delta\mu - \Delta U)]\right)$
Deletion	20	$\min\left(1, \frac{N_A}{N_B + 1} \exp[-\beta(\Delta\mu + \Delta U)]\right)$

4. Results and discussions

4.1 Accuracy of the ANN model

The parity plots in Figure 4 show the ANN predicted probabilities versus probabilities from RMC with the validation dataset. The training and validation results are shown separately in Section S1 of Supporting Information. Excellent agreement is observed for both square and triangular lattice. The values of correlation coefficient R during training and validation is presented in Table 2. Large values of R exceeding 0.999 are obtained. This confirms that $\pi_{AA}(\epsilon; x, z)$ and $\pi_{VA}(\epsilon; x, z)$ are accurately captured by the ANNs in the entire $x - z$ space of interest.

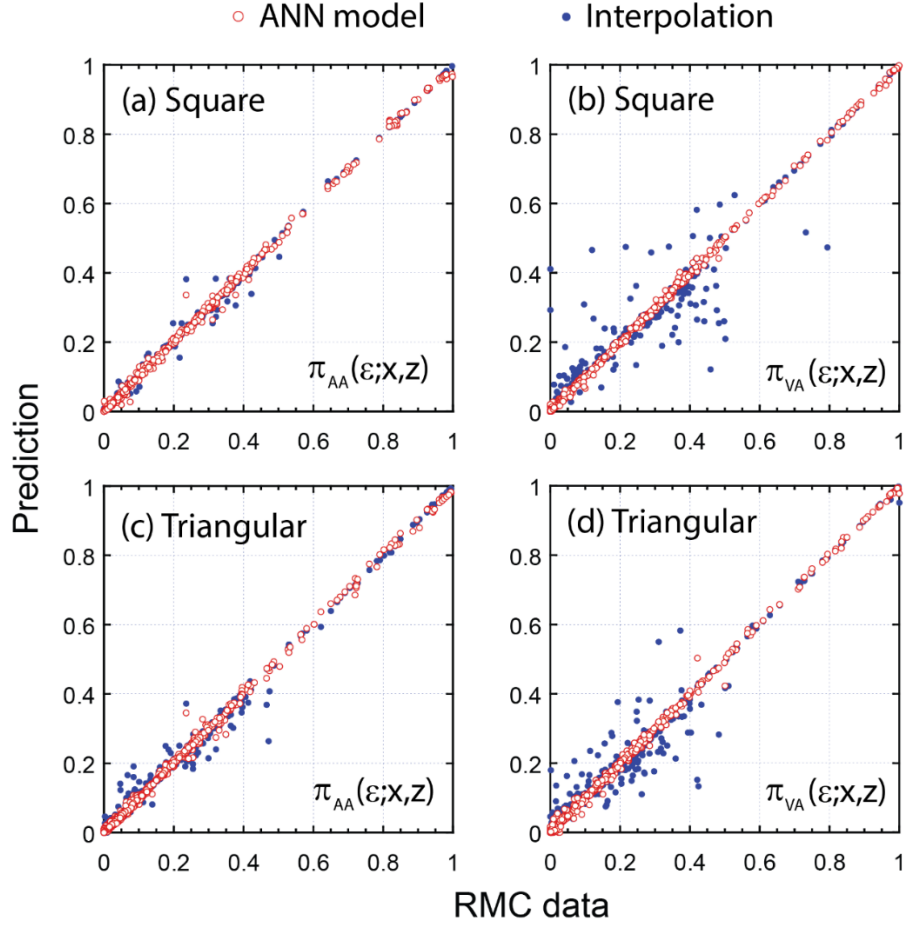


Figure 4: Parity plots showing predicted versus actual probabilities obtained with the validation data. Red open circle and blue filled circles denote ANN and interpolation methods, respectively.

Table 2: R values during training and validation of the ANNs

Lattice	Probability distribution	Training step R	Validation step R	Overall R
Square	π_{AA}	0.9993	0.9994	0.9993
	π_{VA}	0.9997	0.9997	0.9997

Triangular	π_{AA}	0.9992	0.9993	0.9992
	π_{VA}	0.9996	0.9994	0.9995

In general, a large number of data points are required to train an ANN model. However, this issue is not encountered here because the $\pi_{AA}(\epsilon; x, z)$ and $\pi_{VA}(\epsilon; x, z)$ functions do not possess significant undulation. Therefore, it is possible to create a compact ANN model that is reasonably accurate. A comparison of ANN and interpolation scheme shows that the former is superior. Both approaches used the same training data set to predict the probabilities in the validation dataset. Figure 4 shows that the ANN model can achieve reasonable accuracy with fewer data points than the interpolation scheme. The maximum absolute error with the interpolation method using the validation dataset are 0.15 and 0.41 for π_{AA} and π_{VA} of square lattice, respectively. Corresponding error for triangular lattice is 0.21 and 0.3.

π_{AA} and π_{VA} from the ANN models are shown as barplots in Figures 5 and 6. π_{AA} and π_{VA} for a given ϵ can be non-monotonic. For example, see variation in $\pi_{AA}(\epsilon = 2; x = 0.4, z)$ with respect to z in Figure 5. Once again we can see that overall the probabilities are correctly predicted, i.e., the absolute error is small. However, the percentage error is large when the probabilities are small. This is expected since the absolute error is used in the training procedure. Environments associated with small probabilities are more susceptible to sampling errors in RMC since very large lattices or multiple samples are required. The error in Equation (10) due to such π_{AA} and π_{VA} is not amplified, as small probabilities do not contribute significantly.

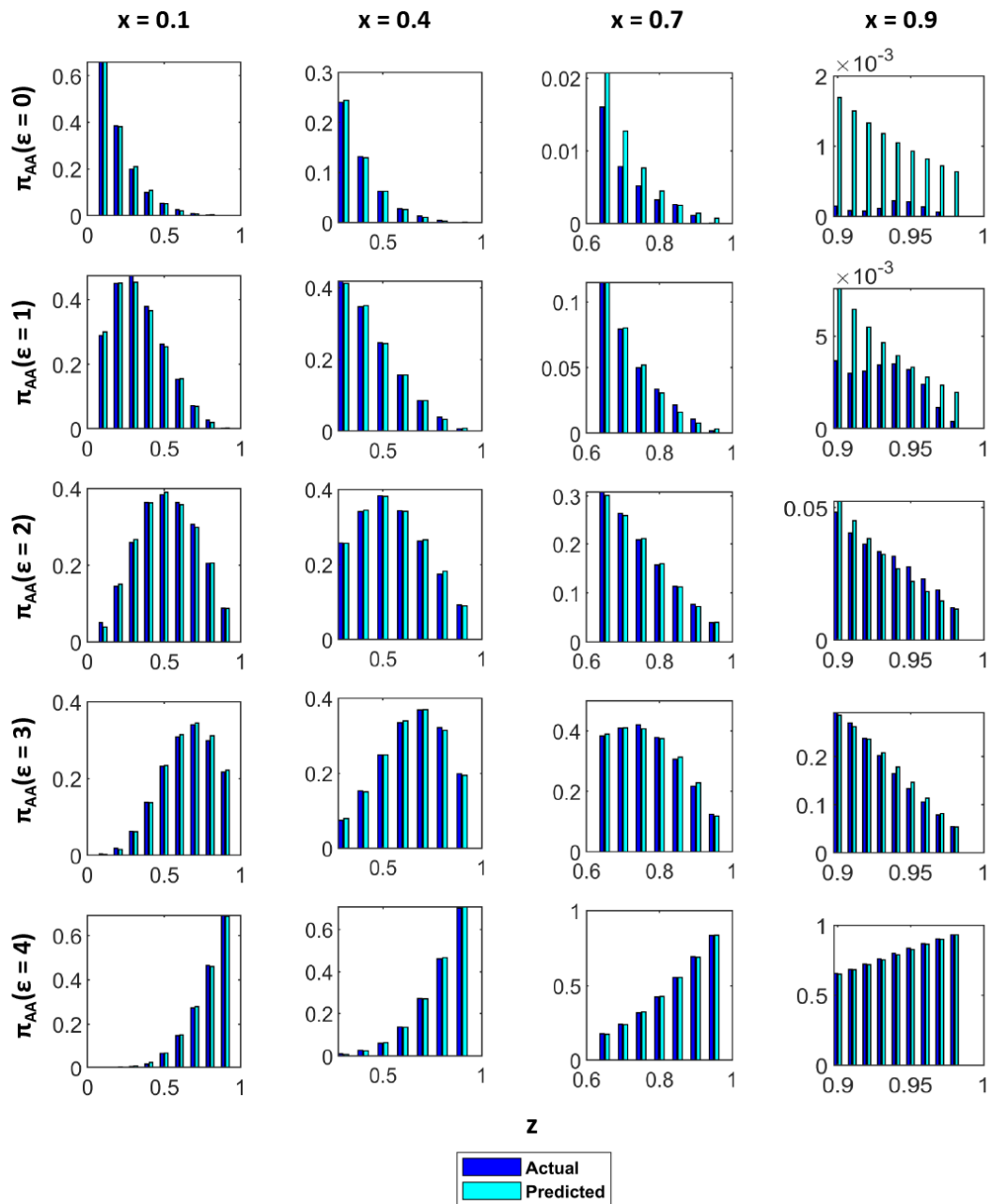


Figure 5: Barplot showing actual and ANN predicted $\pi_{AA}(\epsilon)$ for square lattice.

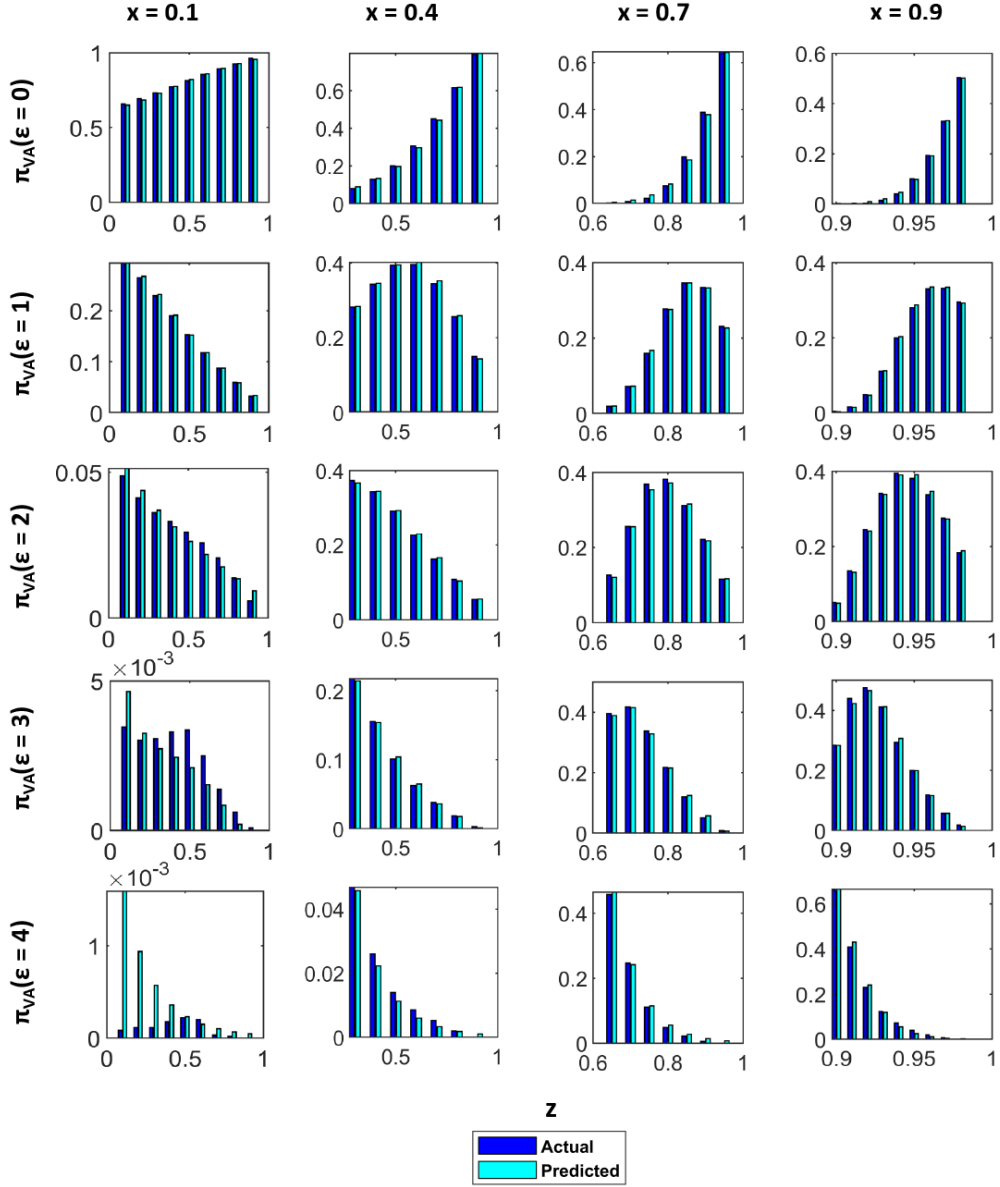


Figure 6: Barplot showing actual and ANN predicted $\pi_{VA}(\epsilon)$ for square lattice.

The variation in probability distributions depends on the region of $x - z$ space under consideration. Therefore, a variable grid size in $x - z$ space is used in Figure 3b. Large variations are observed with dilute/dense systems where x and z take extreme values ($x, z \geq 0.9$). A grid

size as low as 0.001 is used at some locations. A relatively coarser grid of gridsize 0.05 is used for other regions of $x - z$ space.

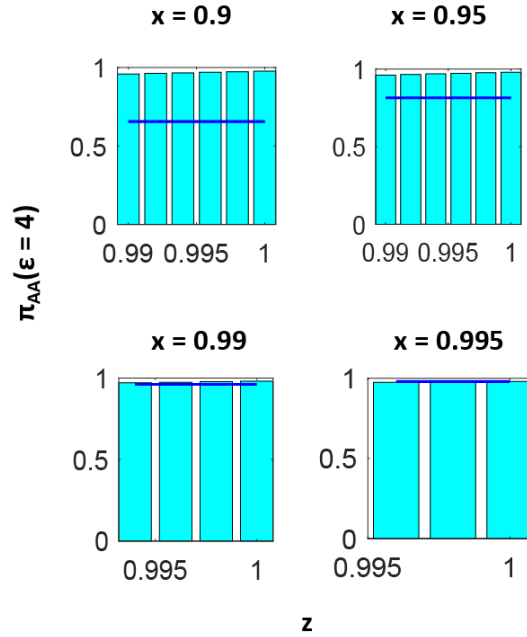


Figure 7: π_{AA} predicted by ANN models in parts of the $x - z$ space for square lattice where RMC calculations do not converge. The blue lines represent probabilities from the binomial distribution.

Recall the region above the dashed line in Figure 3b which is inaccessible to RMC. We explore the ANN behavior when it is extrapolated to $z = 1$ where $x \geq 0.9$. This corresponds to the top-right corner of the $x - z$ space in Figure 3b. In Figure 7, the ANN predicted π_{AA} for square lattice is shown in terms of barplots. The horizontal axis corresponds to z . Only large values of x ($x = 0.9, 0.95, 0.99$ and 0.995) are considered in the panels and $\epsilon = 4$. The largest value of z that were sampled with these x are 0.98, 0.98, 0.993 and 0.995, respectively. From Figure 7 we see

that the ANN model is well-behaved till $z = 1$. Based on these results, we can demarcate the top inaccessible part of $x - z$ space in Figure 3b as $z > 0.334x^3 - 0.6197x^2 + 0.4039x + 0.882$ provided $x < 0.9$. For $x > 0.9$, the ANN model can be used till $z = 1$.

The binomial distribution is generally valid for dilute systems. Blue lines in Figure 7 represent the probabilities based on the binomial distribution $\pi_{AA}^{binomial}(\epsilon) = \frac{c!}{\epsilon!(c-\epsilon)!} x^\epsilon (1-x)^{c-\epsilon}$, $\epsilon \in [0, c]$.

At $x = 0.9$, the ANN predicted $\pi_{AA}(\epsilon = 4)$ is quite different from the binomial distribution. This is because the z values are much larger than x . Therefore, $x = 0.9$ cannot be considered as an ideal system unless $z \approx x$. As x increases, the predicted values approach the binomial distribution for any $z > x$. Good agreement between the ANN model and binomial distribution is observed for $x = 0.995$. Thus, the system can be considered to be ideal for $x \geq 0.995$.

Similar to square lattice, we provide barplots for the actual and ANN predicted probabilities in Figures 8 and 9. Once again, probabilities are correctly predicted. A comparison between Figures 5 and 6 with Figures 8 and 9 reveals that the trends for the square and triangular lattice are quite similar. The values of the probabilities observed with the triangular lattice are slightly lower since more number of ϵ values are possible. For example, when $x = 0.1$ the probability $\pi_{AA}(\epsilon = 0, z = 0.1)$ is 0.62 and 0.5 in case of square and triangular lattices, respectively.

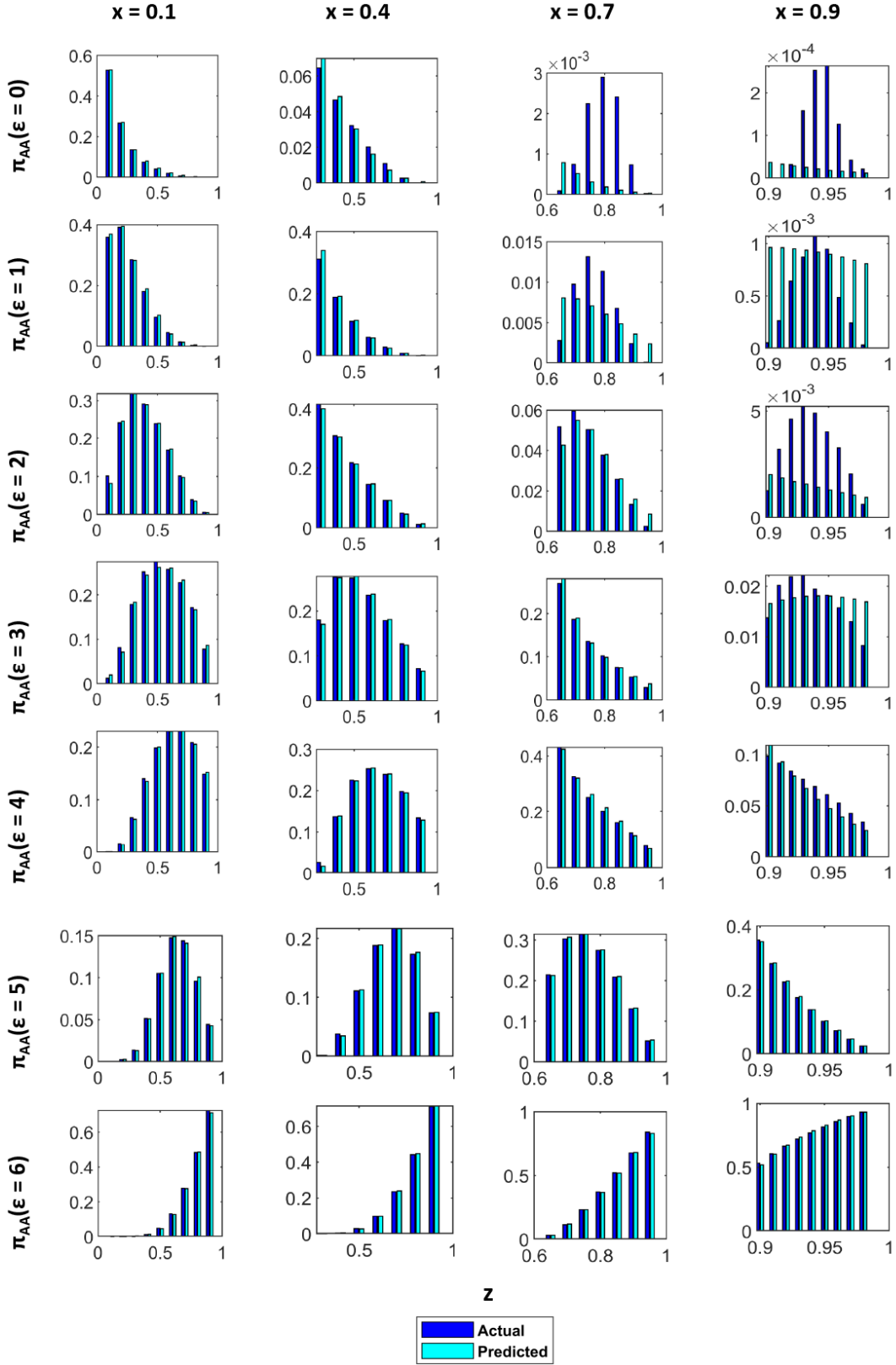


Figure 8: Barplot showing actual and ANN predicted $\pi_{AA}(\epsilon)$ for triangular lattice.

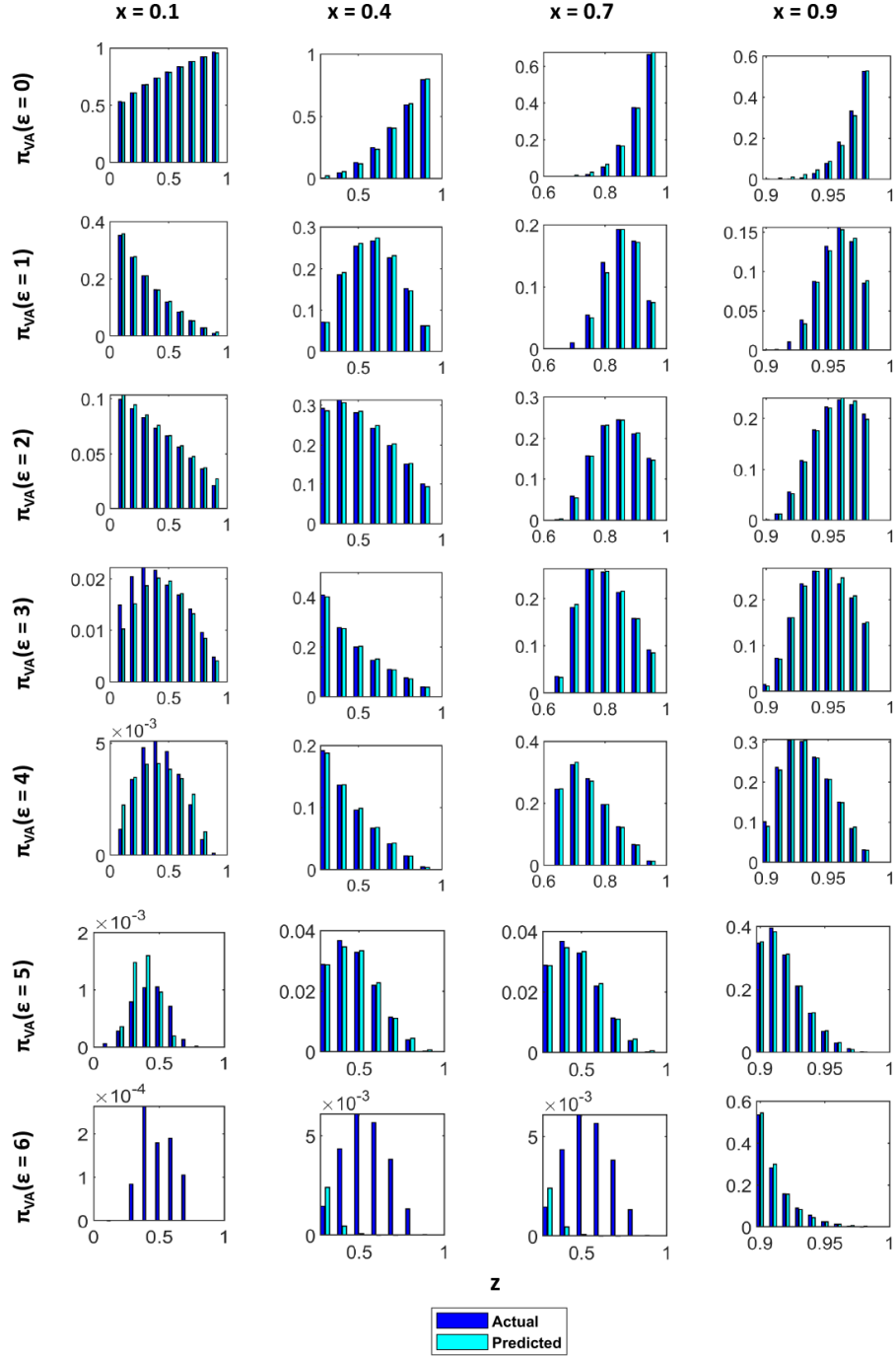


Figure 9: Barplot showing actual and ANN predicted $\pi_{VA}(\epsilon)$ for triangular lattice.

4.2 Net probability flux

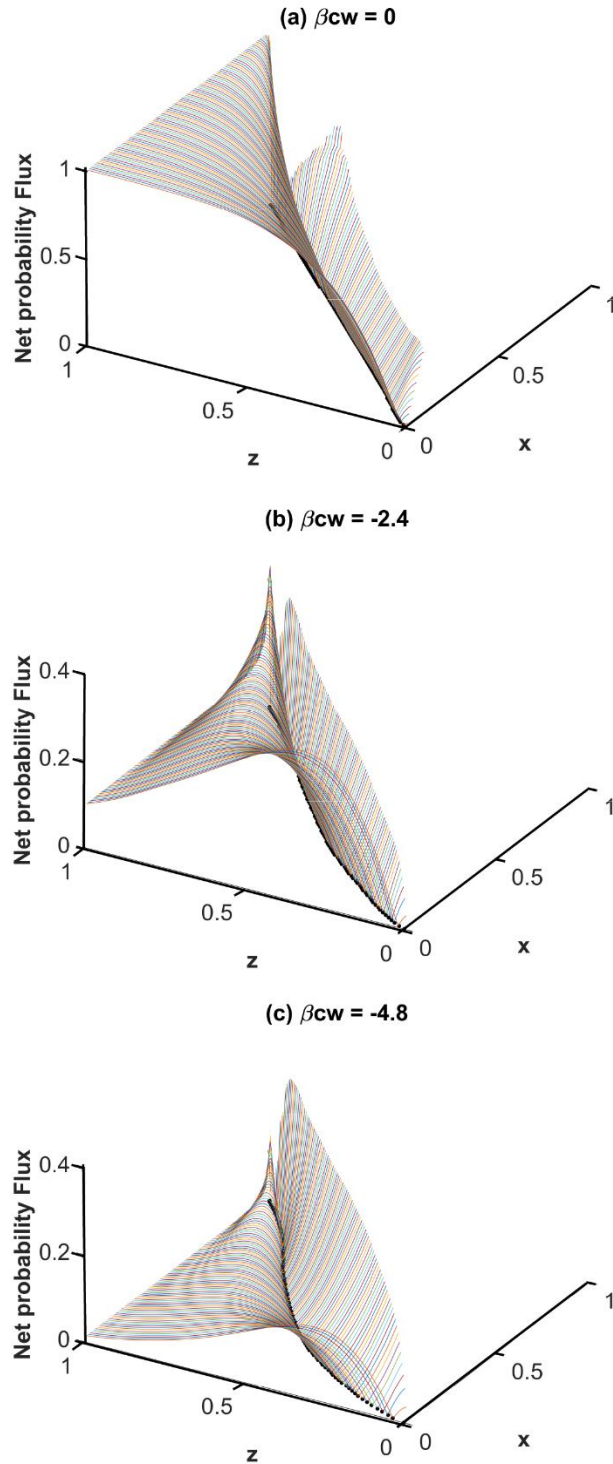


Figure 10: Net probability flux calculated at different temperatures/interactions for square lattice. Black circles denote z_{eq} where the net flux becomes zero.

To illustrate how the equilibrium short-ranged order parameter z_{eq} is evaluated, we use the ANN model for π_{AA} and π_{VA} with Equation (9) to calculate the net probability flux as a function of x and z . The result is presented as 3D line plot in Figure 10 for different β_{cw} . Black circles are the points where the net flux becomes zero, i.e., it yields the $z_{eq}(x, w, T)$. When interactions are absent (panel a), i.e., $\beta_{cw} = 0$, we find $z_{eq} = x$. This is in agreement with our expectation of a perfectly random arrangement of A . For stronger attractive interactions $\beta_{cw} < 0$, z_{eq} is always greater than x implying clustering of A will be observed. Similar results are obtained for triangular lattice (not shown). A MATLAB code illustrating the calculation of z_{eq} and $\Delta\mu$ with square/triangular lattice has been provided in Section S2 of the Supporting Information. Figure 11 shows how z_{eq} varies with x for both lattices. For a given x and β_{cw} , z_{eq} obtained for the triangular lattice is slightly lower than the one for square lattice.

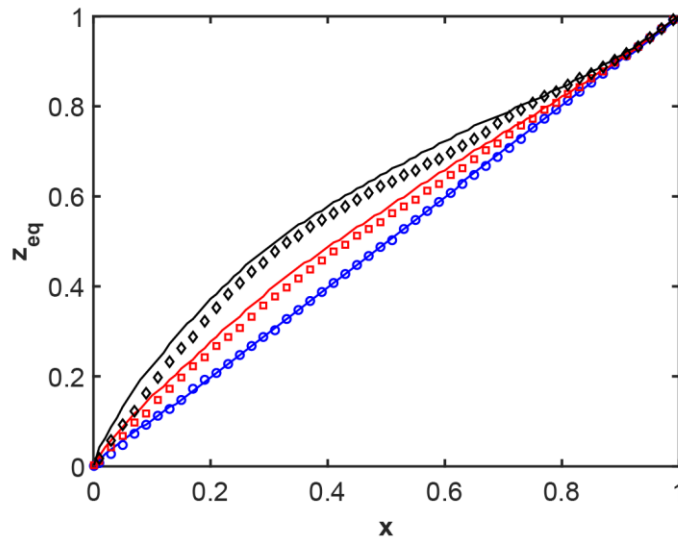


Figure 11: z_{eq} as a function of x . Lines represent square lattice, whereas symbols represent triangular lattice. Blue: $\beta cw = 0$, Red: $\beta cw = -2.4$, Black: $\beta cw = -4.8$.

4.3 Adsorption isotherm

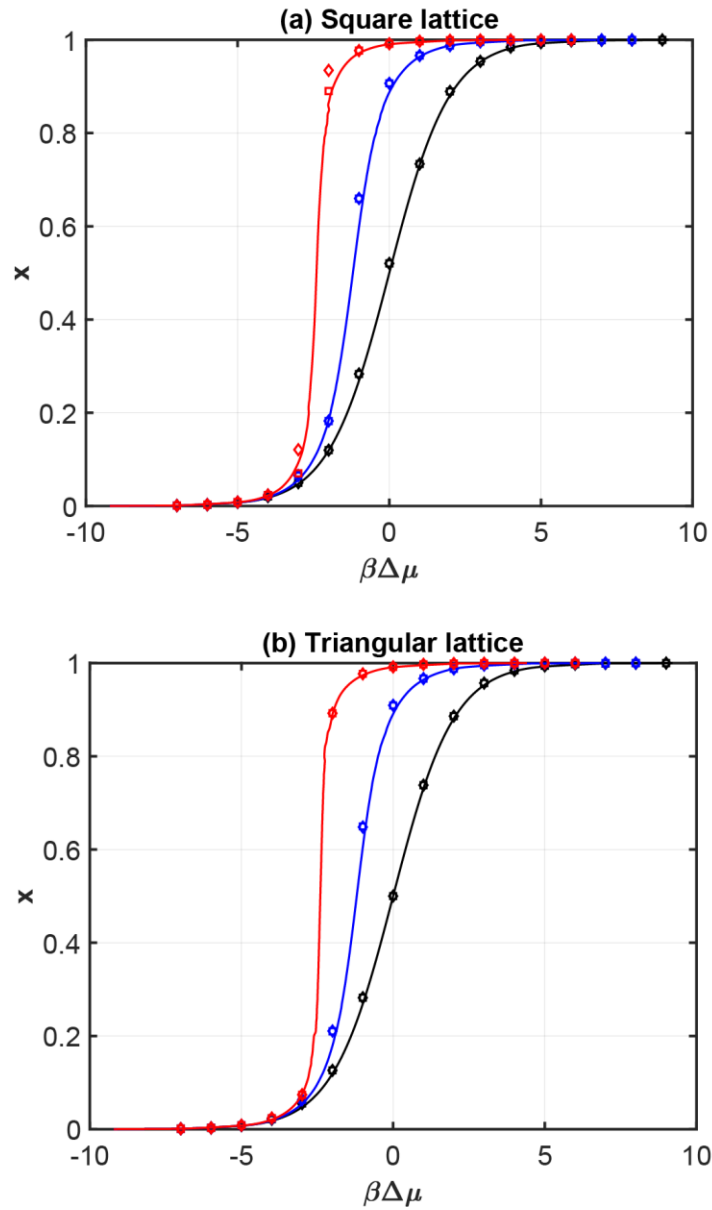


Figure 12: Chemical potential estimation using ANN/RMC (lines) and GCMC (symbols) with varying β_{cw} . Black: $\beta_{cw} = 0$, Blue: $\beta_{cw} = -2.4$, Red: $\beta_{cw} = -4.8$. Square symbols represents GCMC loading calculations, whereas diamond symbols represents unloading.

Transferability and extendibility are two important aspects related to the use of ML models in molecular simulations. A common application involves the prediction of atom-specific information, such as partial charges⁵⁶, force fields⁵⁷, etc. In these applications, transferability refers to the use of the model with any molecular system as long as the properties of constituent atoms can be predicted. Transferability ensures data efficiency, low computational overhead and breadth of application. In the present work, the ANN models for statistical distributions like π_{AA} and π_{VA} are transferable in the sense that they can apply to a number of atomic/molecular systems and a wide range of interactions strengths and temperatures as shown next. Extendibility refers to the use of the model with a system of size larger than the one it was first trained with. The ANN models developed here are extendable. Properties such as energy, free energy changes and number of $A - A$ pairs can be easily estimated for larger system sizes with the same ANN model.

Figure 12 shows the adsorption isotherms generated using ANN/RMC model for β_{cw} between 0 to -4.8. We compare the isotherms with the ones generated using GCMC. In GCMC simulations, one calculates average x at given value of $\beta\Delta\mu$ and β_{cw} . Results for both types of starting structure are shown: pure B (loading) and pure A (unloading). We observe excellent agreement

between the two approaches. The chemical potential $\Delta\mu = \frac{cw}{2}$ at $x = 0.5$ for both square and triangular lattice.

In most systems, the adsorbate-adsorbate interactions w are fixed, whereas the temperature is varied. The values of βcw considered in Figure 12 are in accordance with real systems, e.g., O adsorption on Pd (100) and Pt (111) surfaces. For (100) surface, adsorbed O occupy four-fold hollow sites⁵⁸ which corresponds to a square lattice. Similarly, O occupies the hollow FCC sites at the (111) surface⁵⁹ which corresponds to a triangular lattice. Considering the interactions in O-Pt (111) and O-Pd (100), the range of βcw considered here corresponds to 483 K or higher, respectively. Typical experimental temperatures can be higher.

4.4 Extension to off-lattice systems: H adsorption on Ni (100) surface

Our ANN/RMC approach can be extended to off-lattice system. For this purpose, the surface adsorption for hydrogen on Ni(100) surface is studied. The adsorption isotherm from ANN/RMC and GCMC simulations are compared. The off-lattice GCMC model uses embedded atom method (EAM) potential for the Ni-H system⁶⁰. The EAM interatomic potential provides the interactions between Ni-Ni, H-H and Ni-H atoms. The total potential energy of the system is given by

$$E(r_1, r_2, \dots, r_N) = \sum_{\langle i,j \rangle} \phi_{ij}(r_{ij}) + \sum_i F_i(\rho_i). \quad (12)$$

Here r_i is the coordinate of atom i , ϕ_{ij} denotes the pair potential for i and j (ϕ_{H-H} , ϕ_{Ni-H} or ϕ_{Ni-Ni}), r_{ij} is the separation between atoms i and j , F_i is the embedding energy for atom i , and ρ_i is the density term. ρ_i contains contributions from neighbors of atom i , which makes the EAM a many-body potential.

The LAMMPS code⁶¹ is used to perform the iterative GCMC-MD calculations wherein 1500 GCMC trial moves is followed by 100 molecular dynamics (MD) steps. A total of 9 million trial moves are attempted in the GCMC calculations. The chemical potential of H is specified. The GCMC trial moves consisting of insertion of H, deletion of H and displacement of H are performed with an equal probability. The MD calculation ensures that the overall structure is relaxed. The average H coverage is obtained once the system has equilibrated. From GCMC calculations, we find that H occupies the four-fold hollow site. See the square lattice arrangement at low and high coverages in Figure 13a. It is assumed that the four-fold hollow site is involved with ANN/RMC. Only up to 0.5 ML coverage is studied with GCMC, since two types of sites are found to be occupied at higher coverages⁶².

The EAM interaction cutoff is beyond first nearest neighbor. However, the ANN/RMC framework we have presented employs the 1NN interaction strength w . We exploit the fact that the H-H and H-Ni interaction strength decays fairly quickly with respect to the distance between neighbors. The goal is to obtain an effective interaction parameter w for the H-Ni system. A cluster expansion model⁶³ is constructed to estimate the configurational energy for the ANN/RMC framework:

$$E(\sigma) = \sum_i^{1\text{-body}} V_i \sigma_i + \sum_{i>j}^{2\text{-body}} V_{i,j} \sigma_i \sigma_j + \sum_{i>j>k}^{3\text{-body}} V_{i,j,k} \sigma_i \sigma_j \sigma_k + \dots \quad (13)$$

σ is the occupation vector and for any site i , $\sigma_i = 1$ if the site is occupied by H, otherwise $\sigma_i = 0$. The coefficients in the equation (V s) are the effective cluster interactions (ECI) and they represent contribution from each cluster (1-body, 2-body etc.) to the energy. A large number of random H/Ni(100) configurations were generated. The energy associated with the energy-

minimized configuration was obtained and the ECIs were fitted to such data. V_i ($= -2.82$ eV) corresponds to the binding energy of H. Since the interactions between the adsorbed H-H is weak, only 1 NN pair interactions ($V_{ij} = w = 0.0082$ eV) are included. This allows us to use the ANN model from Section 4.1 for H/Ni(100) adsorption.

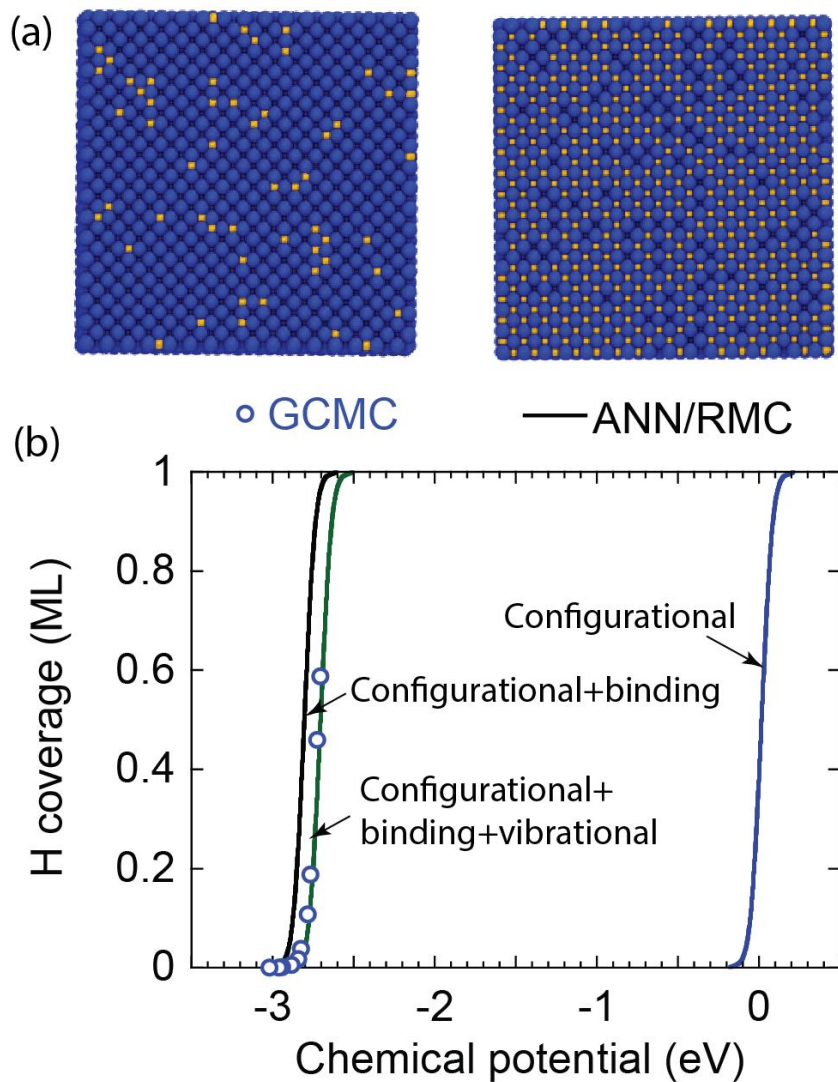


Figure 13: (a) Adsorbed H on Ni (100) surface at 298 K. Blue: Ni; Orange: H. (b) Adsorption isotherm from GCMC (circle) and ANN/RMC (solid lines). For ANN/RMC results with different terms are shown.

It can be shown that for the off-lattice system,

$$\Delta\mu = \mu_{binding} + \mu_{vibrational} + \Delta\mu_{configurational}. \quad (14)$$

$\Delta\mu_{configurational}$ is calculated using Equation (2) or (4). $\mu_{binding}$ arises from H binding to the Ni surface, while $\Delta\mu_{vibrational}$ arises due to the vibrational motion of the H atoms. These terms are calculated as

$$\mu_{binding} = V_i \quad (15)$$

and

$$F_{vib} = \sum_{i=1}^{3N} \left[\frac{h\omega_i}{2} + kT \ln(1 - e^{-h\omega_i/kT}) \right] \quad (16)$$

$$\mu_{vibrational} = \frac{dF_{vib}}{dn}$$

In Equation (16), ω_i is the vibrational frequency obtained using normal mode analysis and h is the Planck's constant. The vibrational frequencies were determined using from the dynamical matrix. F_{vib} was found to be linear with respect to the number of adsorbed H atoms n .

Figure 13 shows the adsorption isotherm obtained by including the different terms. ANN/RMC results are shown in lines, whereas GCMC result is shown in circles. Section S6 of Supporting Information provides the same data in table form. When only the configurational part is included the isotherm is shifted to the right. Including the binding energy term brings the isotherm closer to the GCMC result. However, the inclusion of vibrational term ($\mu_{vibrational} = 0.105 \text{ eV}$) is essential to match with GCMC. The adsorption behaviour is correctly obtained with the ANN/RMC framework when all terms are included.

5. Conclusions

This paper demonstrates application of ANN models in RMC-based thermodynamic calculations. Previously, the RMC-based method required a database/library of configurations for interpolation, so that probability of local atomic arrangements can be obtained. The use of ANN model brings several advantages. First, the database no longer needs to be retained after the model has been fitted, which is the main motivation for this work. The compactness of the ANN model makes implementation of the thermodynamic calculations easier. The MATLAB codes provided as Supporting Information demonstrate these aspects. The ANN model solves a major issue in statistical thermodynamics that analytical, differentiable, closed-form expressions for the probability distributions are often not available. Moreover, as shown in Figure 4 the ANN model is more accurate than the interpolation method while requiring less data. ANN/RMC approach is found to be efficient and accurate in predicting the chemical potentials and adsorption isotherm. We have also extended our approach to off-lattice systems, namely, the H adsorption isotherm on 4-fold hollow sites of Ni (100) surface.

The ANN based approach presented here lays the foundation for extension to more complex lattice structures and longer-ranged interactions, which will be explored in future. There are situations where the single SRO parameter studied here may not be adequate for the problem in question. For example, repulsive lateral interactions can cause the adsorbed species to form ordered structures. It was shown in Ref. ²⁹ that three SRO parameters are required for ordered structures in the NiPt system. Similarly, multiple order parameters are required in case of multiple site types or multisite occupation^{64–68}.

One limitation of the present approach is regarding the choice of sample points for building the training set, viz., which part of the $x - z$ space to sample and how many points. This is linked to the uncertainty in the predictions. Unlike other ML techniques such as Gaussian process regression (GPR)⁵², uncertainty estimates are not available with the present approach. In future, attempts will be made to include the uncertainty using GPR, kriging or Kalman filter techniques. Samples can be added where the uncertainty is high, which could benefit the ANN model construction. Direct use of GPR for thermodynamic calculations may not be advisable as GPR will require dataset at all times, which is contrary to the original goal of this work. Moreover, in GPR the computational time scales as s^3 , where s is the number of samples. The high runtime in GPR is attributed to the inverse calculation of large covariance matrix. In the present study, $s \approx 400$. This number can be easily higher when we consider more complex lattice structures with multiple SRO parameters. Thus, it is hoped that neural networks might continue to be an efficient and reliable tool for training probability distribution functions with more complex problems.

6. Data and Software Availability

Software (MATLAB source code) is freely available at:

<https://sites.google.com/view/abhijit chatterjee/download>.

More description is provided in the Supporting Information.

7. Author contributions

AKB performed RMC calculations, training of the ANN models, GCMC calculations for the lattice systems and was involved in the creation of figures and writing of the manuscript. SR performed

GCMC calculations for the off-lattice system and normal mode analysis. GA was involved in the interpolation method. AC was involved in conceptualization, supervision, development of methodology, writing, reviewing and editing.

8. Acknowledgements

AC acknowledges support from Science and Engineering Research Board, Grant Nos. EMR/2017/001520 and MTR/2019/000909, and National Supercomputing Mission DST/NSM/R&D_HPC_Applications/2021/02.

9. References

- (1) Schütt, K. T.; Arbabzadah, F.; Chmiela, S.; Müller, K. R.; Tkatchenko, A. Quantum-Chemical Insights from Deep Tensor Neural Networks. *Nat. Commun.* **2017**, *8*, 6–13. <https://doi.org/10.1038/ncomms13890>.
- (2) Chmiela, S.; Sauceda, H. E.; Müller, K. R.; Tkatchenko, A. Towards Exact Molecular Dynamics Simulations with Machine-Learned Force Fields. *Nat. Commun.* **2018**, *9* (1). <https://doi.org/10.1038/s41467-018-06169-2>.
- (3) Bernstein, N.; Csányi, G.; Deringer, V. L. De Novo Exploration and Self-Guided Learning of Potential-Energy Surfaces. *npj Comput. Mater.* **2019**, *5* (1), 1–9. <https://doi.org/10.1038/s41524-019-0236-6>.
- (4) Zong, H.; Pilania, G.; Ding, X.; Ackland, G. J.; Lookman, T. Developing an Interatomic Potential for Martensitic Phase Transformations in Zirconium by Machine Learning. *npj Comput. Mater.* **2018**, *4* (1). <https://doi.org/10.1038/s41524-018-0103-x>.

- (5) Pun, G. P. P.; Batra, R.; Ramprasad, R.; Mishin, Y. Physically Informed Artificial Neural Networks for Atomistic Modeling of Materials. *Nat. Commun.* **2019**, *10* (1), 1–10. <https://doi.org/10.1038/s41467-019-10343-5>.
- (6) Elias, J. S.; Artrith, N.; Bugnet, M.; Giordano, L.; Botton, G. A.; Kolpak, A. M.; Shao-Horn, Y. Elucidating the Nature of the Active Phase in Copper/Ceria Catalysts for CO Oxidation. *ACS Catal.* **2016**, *6* (3), 1675–1679. <https://doi.org/10.1021/acscatal.5b02666>.
- (7) Artrith, N.; Kolpak, A. M. Understanding the Composition and Activity of Electrocatalytic Nanoalloys in Aqueous Solvents: A Combination of DFT and Accurate Neural Network Potentials. *Nano Lett.* **2014**, *14* (5), 2670–2676. <https://doi.org/10.1021/nl5005674>.
- (8) Rowe, P.; Csányi, G.; Alfè, D.; Michaelides, A. Development of a Machine Learning Potential for Graphene. *Phys. Rev. B* **2018**, *97* (5), 1–12. <https://doi.org/10.1103/PhysRevB.97.054303>.
- (9) Sawarkar, S.; Chatterjee, A. Decision Tree Driven Construction of Rate Constant Models: Identifying the “Top-N” Environment Atoms That Influence Surface Diffusion Barriers in Ag, Cu, Ni, Pd and Pt. *Comput. Mater. Sci.* **2020**, *184*, 109876. <https://doi.org/https://doi.org/10.1016/j.commatsci.2020.109876>.
- (10) Rosenberger, D.; Barros, K.; Germann, T. C.; Lubbers, N. Machine Learning of Consistent Thermodynamic Models Using Automatic Differentiation. *Phys. Rev. E* **2022**, *105* (4), 45301. <https://doi.org/10.1103/PhysRevE.105.045301>.
- (11) Cats, P.; Kuipers, S.; de Wind, S.; van Damme, R.; Coli, G. M.; Dijkstra, M.; van Roij, R.

- Machine-Learning Free-Energy Functionals Using Density Profiles from Simulations. *APL Mater.* **2021**, *9* (3), 31109. <https://doi.org/10.1063/5.0042558>.
- (12) Craven, G. T.; Lubbers, N.; Barros, K.; Tretiak, S. Machine Learning Approaches for Structural and Thermodynamic Properties of a Lennard-Jones Fluid. *J. Chem. Phys.* **2020**, *153* (10), 104502. <https://doi.org/10.1063/5.0017894>.
- (13) Schneider, E.; Dai, L.; Topper, R. Q.; Drechsel-Grau, C.; Tuckerman, M. E. Stochastic Neural Network Approach for Learning High-Dimensional Free Energy Surfaces. *Phys. Rev. Lett.* **2017**, *119* (15), 150601. <https://doi.org/10.1103/PhysRevLett.119.150601>.
- (14) Hill, T. L. *An Introduction to Statistical Thermodynamics*; Dover: New York, 1986.
- (15) K Binder. Applications of Monte Carlo Methods to Statistical Physics. *Reports Prog. Phys.* **1997**, *60* (5), 487. <https://doi.org/10.1088/0034-4885/60/5/001>.
- (16) Pasinetti, P. M.; Ramirez-Pastor, A. J.; Vogel, E. E.; Saravia, G. Entropy-Driven Phases at High Coverage Adsorption of Straight Rigid Rods on Two-Dimensional Square Lattices. *Phys. Rev. E* **2021**, *104* (5), 54136. <https://doi.org/10.1103/PhysRevE.104.054136>.
- (17) Romá, F.; Ramirez-Pastor, A. J.; Riccardo, J. L. Configurational Entropy for Adsorbed Linear Species (k-Mers). *J. Chem. Phys.* **2001**, *114* (24), 10932–10937. <https://doi.org/10.1063/1.1372187>.
- (18) Phares, A. J.; Wunderlich, F. J.; Grumbine, D. W.; Curley, J. D. The Entropy Curves for Interacting Dimers on a Square Lattice. *Phys. Lett. A* **1993**, *173* (4), 365–368. [https://doi.org/https://doi.org/10.1016/0375-9601\(93\)90251-T](https://doi.org/https://doi.org/10.1016/0375-9601(93)90251-T).

- (19) Phares, A. J.; Wunderlich, F. J. Thermodynamics of Dimers on a Rectangular $L \times M \times N$ Lattice. *J. Math. Phys.* **1985**, *26* (10), 2491–2499. <https://doi.org/10.1063/1.526764>.
- (20) Romá, F.; Ramirez-Pastor, A. J.; Riccardo, J. L. Configurational Entropy in K-Mer Adsorption. *Langmuir* **2000**, *16* (24), 9406–9409. <https://doi.org/10.1021/la000229s>.
- (21) Girardi, M.; Figueiredo, W. A Trimer Model for Water. *J. Chem. Phys.* **2004**, *120* (11), 5285–5292. <https://doi.org/10.1063/1.1648301>.
- (22) Piercy, P.; Debell, K.; Pfñr, H. Phase Diagram and Critical Behavior of the Adsorption System O/Ru(001): Comparison with Lattice-Gas Models. *Phys. Rev. B* **1992**, *45* (4), 1869–1877. <https://doi.org/10.1103/PhysRevB.45.1869>.
- (23) Liu, D.-J. CO Oxidation on Rh(100): Multisite Atomistic Lattice-Gas Modeling. *J. Phys. Chem. C* **2007**, *111* (40), 14698–14706. <https://doi.org/10.1021/jp071944e>.
- (24) Koper, M. T. M. A Lattice-Gas Model for Halide Adsorption on Single-Crystal Electrodes. *J. Electroanal. Chem.* **1998**, *450* (2), 189–201. [https://doi.org/10.1016/S0022-0728\(97\)00648-7](https://doi.org/10.1016/S0022-0728(97)00648-7).
- (25) Koper, M. T. M.; Jansen, A. P. J.; Van Santen, R. A.; Lukkien, J. J.; Hilbers, P. A. J. Monte Carlo Simulations of a Simple Model for the Electrocatalytic CO Oxidation on Platinum. *J. Chem. Phys.* **1998**, *109* (14), 6051–6062. <https://doi.org/10.1063/1.477230>.
- (26) Monroe, J. I.; Hatch, H. W.; Mahynski, N. A.; Shell, M. S.; Shen, V. K. Extrapolation and Interpolation Strategies for Efficiently Estimating Structural Observables as a Function of Temperature and Density. *J. Chem. Phys.* **2020**, *153* (14), 144101.

<https://doi.org/10.1063/5.0014282>.

- (27) Mahynski, N. A.; Errington, J. R.; Shen, V. K. Multivariable Extrapolation of Grand Canonical Free Energy Landscapes. *J. Chem. Phys.* **2017**, *147* (23), 234111. <https://doi.org/10.1063/1.5006906>.
- (28) Mahynski, N. A.; Errington, J. R.; Shen, V. K. Temperature Extrapolation of Multicomponent Grand Canonical Free Energy Landscapes. *J. Chem. Phys.* **2017**, *147* (5), 54105. <https://doi.org/10.1063/1.4996759>.
- (29) Agrahari, G.; Chatterjee, A. Speed-up of Monte Carlo Simulations by Preparing Starting off-Lattice Structures That Are Close to Equilibrium. *J. Chem. Phys.* **2020**, *152* (4), 44102. <https://doi.org/10.1063/1.5131303>.
- (30) Agrahari, G.; Chatterjee, A. Thermodynamic Calculations Using Reverse Monte Carlo. *Phys. Rev. E* **2021**, *104*, 044129.
- (31) Agrahari, G.; Chatterjee, A. Thermodynamic Calculations Using Reverse Monte Carlo: Convergence Aspects, Sources of Error and Guidelines for Improving Accuracy. *Mol. Simul.* **2022**, *48* (13), 1143–1154.
- (32) Dou, M.; Fyta, M. Lithium Adsorption on 2D Transition Metal Dichalcogenides: Towards a Descriptor for Machine Learned Materials Design. *J. Mater. Chem. A* **2020**, *8* (44), 23511–23518. <https://doi.org/10.1039/D0TA04834H>.
- (33) Hakala, M.; Kronberg, R.; Laasonen, K. Hydrogen Adsorption on Doped MoS₂ Nanostructures. *Sci. Rep.* **2017**, *7* (1), 15243. <https://doi.org/10.1038/s41598-017-15622->

z.

- (34) Sun, Y.; DeJaco, R. F.; Siepmann, J. I. Deep Neural Network Learning of Complex Binary Sorption Equilibria from Molecular Simulation Data. *Chem. Sci.* **2019**, *10* (16), 4377–4388. <https://doi.org/10.1039/C8SC05340E>.
- (35) Yue, S.; Muniz, M. C.; Calegari Andrade, M. F.; Zhang, L.; Car, R.; Panagiotopoulos, A. Z. When Do Short-Range Atomistic Machine-Learning Models Fall Short? *J. Chem. Phys.* **2021**, *154* (3), 341111. <https://doi.org/10.1063/5.0031215>.
- (36) Desgranges, C.; Delhommelle, J. Ensemble Learning of Partition Functions for the Prediction of Thermodynamic Properties of Adsorption in Metal–Organic and Covalent Organic Frameworks. *J. Phys. Chem. C* **2020**, *124* (3), 1907–1917. <https://doi.org/10.1021/acs.jpcc.9b07936>.
- (37) Jablonka, K. M.; Ongari, D.; Moosavi, S. M.; Smit, B. Big-Data Science in Porous Materials: Materials Genomics and Machine Learning. *Chem. Rev.* **2020**, *120* (16), 8066–8129. <https://doi.org/10.1021/acs.chemrev.0c00004>.
- (38) Rahimi, M.; Moosavi, S. M.; Smit, B.; Hatton, T. A. Toward Smart Carbon Capture with Machine Learning. *Cell Reports Phys. Sci.* **2021**, *2* (4), 100396. <https://doi.org/https://doi.org/10.1016/j.xcrp.2021.100396>.
- (39) McGreevy, R. L. Reverse Monte Carlo Modelling. *J. Phys. Condens. Matter* **2001**, *13* (46), R877–R913. <https://doi.org/10.1088/0953-8984/13/46/201>.
- (40) Wikfeldt, K. T.; Leetmaa, M.; Ljungberg, M. P.; Nilsson, A.; Pettersson, L. G. M. On the

- Range of Water Structure Models Compatible with X-Ray and Neutron Diffraction Data. *J. Phys. Chem. B* **2009**, *113* (18). <https://doi.org/10.1021/jp9007619>.
- (41) Harsányi, I.; Pusztai, L. Hydration Structure in Concentrated Aqueous Lithium Chloride Solutions: A Reverse Monte Carlo Based Combination of Molecular Dynamics Simulations and Diffraction Data. *J. Chem. Phys* **2012**, *137*, 204503. <https://doi.org/10.1063/1.4767437>.
- (42) Howe, M. A.; McGreevy, R. L.; Pusztai, L.; Borzsák, & I. Determination of Three Body Correlations in Simple Liquids by RMC Modelling of Diffraction Data. *Phys. Chem. Liq.* **1993**, *25* (4), 205–241. <https://doi.org/10.1080/00319109308030363>.
- (43) Veglio, N.; Bermejo, F. J.; Pardo, L. C.; Li Tamarit, J.; Cuello, G. J. Direct Experimental Assessment of the Strength of Orientational Correlations in Polar Liquids. *Phys. Rev. E* **2005**. <https://doi.org/10.1103/PhysRevE.72.031502>.
- (44) McGreevy, R.L.; Pusztai L. The Structure of Molten Salts. *Proc. R. Soc. London. Ser. A Math. Phys. Sci.* **1990**, *430* (1878), 241–261. <https://doi.org/10.1098/RSPA.1990.0090>.
- (45) Kaban, I.; Jóvári, P.; Stoica, M.; Eckert, J.; Hoyer, W.; Beuneu, B. Topological and Chemical Ordering in Co₄₃Fe₂₀Ta_{5.5}B_{31.5} Metallic Glass. *Phys. Rev. B* **2122**, 79. <https://doi.org/10.1103/PhysRevB.79.212201>.
- (46) Keen, D. A.; McGreevy, R. L. Structural Modelling of Glasses Using Reverse Monte Carlo Simulation. *Nature* **1990**, *344* (6265), 423. <https://doi.org/10.1038/344423a0>.
- (47) Keen, D. A.; Tucker, M. G.; Dove, M. T. Reverse Monte Carlo Modelling of Crystalline

- Disorder. *J. Phys. Condens. Matter* **2005**, *17* (5), S15–S22. <https://doi.org/10.1088/0953-8984/17/5/002>.
- (48) McGreevy, R. L.; Pusztai, L. Reverse Monte Carlo Simulation: A New Technique for the Determination of Disordered Structures. *Mol. Simul.* **1988**, *1* (6), 359–367. <https://doi.org/10.1080/08927028808080958>.
- (49) Lyubartsev, A. P.; Laaksonen, A. Calculation of Effective Interaction Potentials from Radial Distribution Functions: A Reverse Monte Carlo Approach. *Phys. Rev. E* **1995**, *52* (4), 3730–3737. <https://doi.org/10.1103/PhysRevE.52.3730>.
- (50) Playford, H. Y.; Owen, L. R.; Levin, I.; Tucker, M. G. *New Insights into Complex Materials Using Reverse Monte Carlo Modeling*; 2014; Vol. 44. <https://doi.org/10.1146/annurev-matsci-071312-121712>.
- (51) Metropolis, N.; Rosenbluth, A. W.; Rosenbluth, M. N.; Teller, A. H.; Teller, E. Equation of State Calculations by Fast Computing Machines. *J. Chem. Phys.* **1953**, *21* (6), 1087–1092. <https://doi.org/10.1063/1.1699114>.
- (52) Murphy, K. P. *Machine Learning: A Probabilistic Perspective*; The MIT Press: Cambridge, Massachusetts, 2012.
- (53) Verma, S.; Rehman, T.; Chatterjee, A. A Cluster Expansion Model For Rate Constants Of Surface Diffusion Processes On Ag, Al, Cu, Ni, Pd And Pt (100) Surfaces. *Surf. Sci.* **2013**, *613*, 114–125.
- (54) Nguyen, D.; Widrow, B. Improving the Learning Speed of 2-Layer Neural Networks by

- Choosing Initial Values of the Adaptive Weights. In *1990 IJCNN International Joint Conference on Neural Networks*; 1990; pp 21–26 vol.3.
<https://doi.org/10.1109/IJCNN.1990.137819>.
- (55) Frenkel, D.; Smit, B. *Understanding Molecular Simulation: From Algorithms to Applications*; Academic Press: New York, 1996.
- (56) Sifain, A. E.; Lubbers, N.; Nebgen, B. T.; Smith, J. S.; Lokhov, A. Y.; Isayev, O.; Roitberg, A. E.; Barros, K.; Tretiak, S. Discovering a Transferable Charge Assignment Model Using Machine Learning. *J. Phys. Chem. Lett.* **2018**, *9* (16), 4495–4501.
<https://doi.org/10.1021/acs.jpcllett.8b01939>.
- (57) Smith, J. S.; Isayev, O.; Roitberg, A. E. ANI-1: An Extensible Neural Network Potential with DFT Accuracy at Force Field Computational Cost. *Chem. Sci.* **2017**, *8* (4), 3192–3203.
<https://doi.org/10.1039/C6SC05720A>.
- (58) Zhang, Y.; Blum, V.; Reuter, K. Accuracy of First-Principles Lateral Interactions: Oxygen at Pd(100). **2007**, No. March, 1–14. <https://doi.org/10.1103/PhysRevB.75.235406>.
- (59) Tang, H.; Ven, A. Van Der; Trout, B. L.; Tang, H.; Ven, A. V. A. N. D. E. R.; Trout, B. L. Lateral Interactions between Oxygen Atoms Adsorbed on Platinum (111) by First Principles Lateral Interactions between Oxygen Atoms Adsorbed on Platinum (111) by First Principles. *Mol. Phys.* **2004**, *102*, 273–279.
<https://doi.org/10.1080/0026897042000178088>.
- (60) Angelo, J. E.; Moody, N. R.; Baskes, M. I. Trapping of Hydrogen to Lattice Defects in

- Nickel. *Model. Simul. Mater. Sci. Eng.* **1995**, 3 (3), 289–307.
<https://doi.org/10.1088/0965-0393/3/3/001>.
- (61) Plimpton, S. Fast Parallel Algorithms for Short-Range Molecular Dynamics. *J. Comput. Phys.* **1995**, 117, 1–19.
- (62) Rana, S.; Masli, N.; Monder, D. S.; Chatterjee, A. Hydriding Pathway for Ni Nanoparticles: Computational Characterization Provides Insights into the Nanoparticle Size and Facet Effect on Layer-by-Layer Subsurface Hydride Formation. *Comput. Mater. Sci.* **2022**, 210, 111482. <https://doi.org/https://doi.org/10.1016/j.commatsci.2022.111482>.
- (63) Fontaine, D. De. Cluster Approach to Order-Disorder Transformations in Alloys; Ehrenreich, H., Turnbull, D., Eds.; Academic Press, 1994; Vol. 47, pp 33–176.
[https://doi.org/https://doi.org/10.1016/S0081-1947\(08\)60639-6](https://doi.org/https://doi.org/10.1016/S0081-1947(08)60639-6).
- (64) Sanchez-Varretti, F. O.; Bulnes, F. M.; Ramirez-Pastor, A. J. Order and Disorder in the Adsorption Model of Repulsively Interacting Binary Mixtures on Triangular Lattices: Theory and Monte Carlo Simulations. *Eur. Phys. J. E* **2021**, 44 (3), 42.
<https://doi.org/10.1140/epje/s10189-021-00037-6>.
- (65) Fefelov, V. F.; Myshlyavtsev, A. V; Myshlyavtseva, M. D. Complete Analysis of Phase Diversity of the Simplest Adsorption Model of a Binary Gas Mixture for All Sets of Undirected Interactions between Nearest Neighbors. *Adsorption* **2019**, 25 (3), 545–554.
<https://doi.org/10.1007/s10450-019-00043-3>.
- (66) Fefelov, V. F.; Myshlyavtsev, A. V; Myshlyavtseva, M. D. Phase Diversity in an Adsorption

Model of an Additive Binary Gas Mixture for All Sets of Lateral Interactions. *Phys. Chem. Chem. Phys.* **2018**, *20* (15), 10359–10368. <https://doi.org/10.1039/C7CP08426A>.

(67) Dávila, M.; Romá, F.; Riccardo, J. L.; Ramirez-Pastor, A. J. Quasi-Chemical Approximation for Polyatomics: Statistical Thermodynamics of Adsorption. *Surf. Sci.* **2006**, *600* (10), 2011–2025. <https://doi.org/https://doi.org/10.1016/j.susc.2006.02.032>.

(68) González, J. E.; Ramirez-Pastor, A. J.; Pereyra, V. D. Adsorption of Dimer Molecules on Triangular and Honeycomb Lattices. *Langmuir* **2001**, *17* (22), 6974–6980. <https://doi.org/10.1021/la010465i>.

TOC image

